Distinct tau filament folds in familial frontotemporal dementia due to the *MAPT* S305I mutation

Authors: Henry S. Pan[1†], Gregory E. Merz[2,3†], Alissa Nana Li[4], Minh Quan Le[2,5], Hyunil Jo[1], Athena Quddus[2], Anthony Yung[2], Rian C. Kormos[1,5††], Arthur A. Melo[2], Eliana Marisa Ramos[6], Argentina Lario Lago[4], Salvatore Spina[4], Lea T. Grinberg[4,7†††], Howard J. Rosen[4], Eric Tse[2,3], Maria Luisa Gorno-Tempini[4], William F. DeGrado[1], William W. Seeley[4,7]*, and Daniel R. Southworth[2,8]*

Affiliations:

[1]Department of Pharmaceutical Chemistry, The Cardiovascular Research Institution, University of California San Francisco, San Francisco, CA, USA

[2]Institute for Neurodegenerative Diseases, Weill Institute for Neurosciences, University of California San Francisco, San Francisco, CA, USA

[3]Department of Neurology, University of California San Francisco, San Francisco, CA, USA

[4]Weill Institute for Neurosciences, Memory and Aging Center, Department of Neurology, University of California San Francisco, San Francisco, CA, USA

[5]Graduate Program in Biophysics, University of California San Francisco, San Francisco, CA, USA.

[6]Department of Neurology, David Geffen School of Medicine, University of California Los Angeles, Los Angeles, CA, USA

[7]Department of Pathology, University of California San Francisco, San Francisco, CA, USA

[8]Department of Biochemistry and Biophysics, University of California San Francisco, San Francisco, CA, USA

[†]Henry S. Pan and Gregory E. Merz contributed equally to this work.

[††]Present address: St. Jude Children's Hospital, Memphis, TN, USA

[†††]Present address: Departments of Laboratory Medicine and Pathology and Neurosciences, Mayo Clinic Florida, Jacksonville, FL, USA

*Correspondence: Daniel R. Southworth, daniel.southworth@ucsf.edu and William W. Seeley, bill.seeley@ucsf.edu

Abstract

Frontotemporal lobar degeneration with tau inclusions (FTLD-tau) comprise a class of fatal heterogeneous neurodegenerative diseases. Approximately 10% arise from pathogenic MAPT mutations and often cause severe, early-onset disease with pathology that is distinct yet partially overlapping with sporadic cases. Here, we evaluated post-mortem tissue from a patient with FTLD-tau due to *MAPT* S305I showing neuropathology most consistent with argyrophilic grain disease (AGD), a prevalent limbic tauopathy of aging. Structures determined by cryo-electron microscopy reveal tau filament folds that differ from those found in sporadic AGD or other tauopathies and feature a 4-layer architecture stabilized by the Ile substitution within its core. Comparative structural analysis reveals conserved motifs are shared among AGD, corticobasal degeneration, and *MAPT* P301T. A well-defined density stacks along a cationic cleft, indicative of a bound RNA-like polyanion or small-molecule. *In vitro* analysis shows the S305I mutation promotes fibrilization relative to normal tau. These results demonstrate that *MAPT S305I* stabilizes a distinct aggregation-prone tau fold

that likely contributes to disease pathology and heterogeneity beyond its known splicing defects, and underscore potential limitations of using the most pathologically similar genetic form as a model for sporadic FTLD-tau.

Introduction

Tauopathies, including Alzheimer's disease (AD), progressive supranuclear palsy (PSP), corticobasal degeneration (CBD) and others, are a diverse group of neurodegenerative diseases characterized by the accumulation of toxic protein deposits in the brain comprised primarily of the microtubule-associated protein tau (MAPT, or tau)[1–9]. Cryo-electron microscopy (cryo-EM) studies of tau filaments extracted from post-mortem patient brain tissue have revealed that the structural core, which typically includes microtubule-binding repeat domains (R1-R4) and a portion of the C-terminus (C) adopts different cross-β amyloid folds in disease[10–17]. These insights have advanced disease classification by identifying specific types of tau filament folds that arise in different pathologically defined tauopathies[10]. Moreover, the diversity of tau filament structures indicates different molecular mechanisms likely underlie tau aggregation in these diseases. Nonetheless, the molecular and pathological factors that drive the formation of a particular tau disease fold remain poorly understood.

Investigations of pathogenic *MAPT* variants have established the central role of tau aggregation in disease[18] and offer important insight into the molecular drivers of tau filament folds. While most tauopathies occur sporadically[19], more than 60 familial mutations in *MAPT* have been identified to date, each associated with a mutation-specific pattern of frontotemporal lobar degeneration with tau pathology (FTLD-tau)[20]. The observed FTLD-tau pathomorphological features overlap with those seen in the sporadic forms, including AD, PSP, CBD, Pick's disease (PiD), and argyrophilic grain disease (AGD)[10,21–23], prompting some authors to propose that sporadic FTLD-tau can be effectively modeled using familial *MAPT* mutations[24]. Mutations at residue P301, including

74 P301L and P301S, are known to enhance tau aggregation and seeding and are widely
75 used in cell and transgenic animal models for tauopathies, including AD[25–29]. Cryo-EM
76 studies have revealed that familial tau mutations form specific filament folds: P301L and
77 P301T adopt unique structures[30], while V337M and R406W are similar to the AD paired
78 helical filament (PHF) fold[14]. However, only a limited number of tau structures from
79 patients with *MAPT* mutations have been characterized, despite strong interest in defining
80 tau folds that arise in disease and advancing the development of small-molecule
81 diagnostics and therapeutics that selectively bind specific folds[31–33].

82 Familial mutations in *MAPT* occur in both exonic and intronic regions, including
83 several at the exon 10 splice junction, which contains a stem loop regulatory element
84 required for alternative splicing of 3-repeat (3R) and 4-repeat (4R) tau isoforms[34] (**Fig.**
85 **1a**). Mutations in this region cause splicing defects that increase 4R tau levels[35,36] and
86 are proposed to drive 4R-predominant tauopathies resembling CBD and PSP. The *S305I*
87 mutation, located within the coding sequence at the exon 10 splice junction, was
88 previously identified in a patient with severe early onset FTD, with symptoms developing
89 at age 39 and a rapid, 1.5-year disease course[37]. Post-mortem analysis revealed
90 neuropathology similar to sporadic AGD, with argyrophilic grains, neuronal cytoplasmic
91 inclusions, and oligodendroglial coiled bodies comprised of 4R tau, while classical
92 neurofibrillary tangles, Pick bodies, and other tau morphologies were absent[37]. Sporadic
93 AGD is the second most common tauopathy after AD[38], and it is characterized by a very
94 late age of onset and pathology that is typically limited to the limbic system, in contrast to
95 the tauopathy resulting from *S305I* in which tau aggregation is more widespread in frontal
96 and temporal regions,[37] thereby producing an FTD-like clinical picture. Because inherited

97 forms of FTLD-tau have been proposed as models for sporadic FTLD-tau subtypes[24], it
98 is important to determine whether the inherited and sporadic forms are associated with
99 the same underlying tau filament fold.

100 Here, we sought to characterize the neuropathology and tau filament structures
101 from a 39-year-old patient with the *MAPT S305I* mutation. Histopathological analysis
102 revealed tau aggregates with morphological similarities to sporadic AGD but with more
103 severe pathology, extending into the frontal and temporal cortices. Cryo-EM structures of
104 tau filaments isolated from post-mortem tissue were determined to 3.1 and 3.2 Å
105 resolution and demonstrate that S305I tau adopts two unique single protofilament folds.
106 Each is comprised of an identical 4-layer fold and β hairpin involving microtubule repeat
107 domains R2-R4, as well as an R1:C arm arranged differently in the two structures. The
108 S305I residue contributes to the overall fold by packing in a solvent-inaccessible
109 hydrophobic pocket in the center of the 4-layer core. Notably, a distinct unassigned
110 density is resolved along a solvent-facing cleft formed by basic residues in R2 and R3
111 that is suggestive of a cellular polyanion, such as RNA, or a stacking anionic metabolite.
112 Finally, *in vitro* fibrilization analysis of recombinant tau protein containing the S305I
113 mutation reveals more rapid poly-phosphate-induced aggregation relative to normal tau,
114 indicating the mutation alone contributes to tau aggregation. These results reveal that the
115 *MAPT* S305I mutation results in a distinct 4R tau filament fold not previously observed in
116 other sporadic or familial tauopathies. Moreover, S305I may contribute to the unique
117 early-onset AGD-like pathology through accelerated aggregation and promotion of a
118 specific tau filament fold, in addition to previously reported splicing defects and increased
119 4R tau levels.

120

121 **Results**

122 ***MAPT S305I* FTLD-tau Case with Distinct and AGD-like Neuropathological Features**

123 Here, we studied a 39-year-old woman who developed subtle changes in social
124 behavior at age 35, followed by difficulties with speech, spelling, and grammar, prompting
125 a diagnosis of nonfluent variant primary progressive aphasia. Later, she developed more
126 widespread cognitive deficits, including memory loss. Brain MRI revealed severe grey
127 and white matter atrophy most notable in dorsal and opercular frontal, medial temporal,
128 insular, inferior parietal, and limbic structures (**Fig. 1b**). These findings are unlike those
129 typically associated with sporadic AGD, in that less severe atrophy and more focal limbic
130 atrophy is seen (**Fig. 1c**). Her father was diagnosed with FTD in his 50s. *MAPT S305I*
131 was uncovered via research-based genetic screening that included *MAPT*, *APP,*
132 *C9ORF72, FUS, GRN, MAPT, PSEN1, PSEN2* and *TARDBP* genes, as described
133 previously[39,40]. Autopsy was performed ~13 hours after death, and the fresh brain
134 weighed 1000 grams. Hematoxylin and eosin staining of post-mortem brain tissue
135 revealed severe degenerative changes in the frontal operculum, dorsal frontal regions,
136 and angular gyrus that were more pronounced than typically seen in AGD[37], as well as
137 mild to moderate changes in ventral frontal and temporal areas. Immunohistochemistry
138 for hyperphosphorylated tau (CP13 antibody) revealed a pattern of fine argyrophilic grains
139 and threads in both cortical and subcortical regions, along with diffuse/granular neuronal
140 cytoplasmic inclusions, at times with perinuclear halos, occasional compact round
141 neuronal cytoplasmic inclusions, and coiled bodies in areas exhibiting degenerative
142 changes (**Fig. 1d-j**). These features are similar but distinct from those seen in sporadic

143 AGD (**Fig. 1l-q**). Granular/fuzzy astrocytes, a common though not universal feature of
144 sporadic AGD, were absent[41]. An antibody against 3-repeat tau (RD3) disclosed normal
145 findings, confirming the 4-repeat nature of the tauopathy. While these morphological
146 findings are consistent with the previous characterization of a patient with the same *MAPT*
147 *S305I* mutation[37], we conclude that overall, *MAPT S305I* results in certain distinct
148 neuropathological features compared to AGD.
149

150 **S305I Tau Filament Structures Adopt a Unique 4-Layer Fold**

151 We next sought to characterize and determine structures of tau filaments isolated
152 from the patient with *MAPT S305I* described above using cryo-EM. Sarkosyl-insoluble
153 filaments were purified from 1g of fresh-frozen inferior frontal gyrus (IFG) tissue, as
154 previously described[10] (see Methods), and verified by negative-stain and cryo-EM to
155 contain predominantly tau filaments with a wavy morphology (**Fig. 2a and Extended Data**
156 **Fig. 1a-b**). Two-dimensional (2D) class averages exhibit filaments with two distinct
157 morphologies (hereafter referred to as S305I tau Type I and Type II), based on the twist
158 and a crossover distance, measured to be ~600 Å for Type I and ~750 Å Type II (**Fig. 2b**),
159 each with well-defined 4.8 Å β-sheet spacing (**Extended Data Fig. 1c**). Notably, the
160 crossover distances are considerably shorter than for sporadic AGD tau Types I and II,
161 which are reported to be 240 nm and 216 nm, respectively[10]. Following 3D classification
162 and helical reconstruction, we determined structures of S305I tau Type I and Type II
163 filaments at resolutions of 3.1 Å and 3.2 Å, respectively, revealing two distinct filament
164 folds that had not been previously reported (**Fig. 2c, Extended Data Fig. 1d-f, and Table**

165 **1**). Type I constituted the majority (~85%) of the dataset, whereas Type II filaments were
166 less abundant (~15%).

167 The maps for both Type I and II filaments exhibit continuous, well-resolved density
168 with side chain features, revealing both adopt a central 4-layered fold with an exposed
169 hairpin on one face and a lower resolution stem at the opposite face that is positioned
170 differently in each structure (**Fig. 2c**). Notably, a small but well-resolved discontinuous
171 density is identified in a solvent exposed cleft of the 4-layer fold (discussed below).
172 Human 4R tau residues G273–R379 were modeled into the map using Isolde[42] based on
173 a ModelAngelo[43] predicted fit, revealing they form a large 97-residue folded hairpin
174 established by distal cross-β contacts between R2 I277 and C I371 (**Fig. 3a-c**). The 4-
175 layer core is comprised of R2-R4, with the entire length of R4 (residues 337-368) forming
176 the solvent exposed face, contacting R2 (residues 275-285) and R3 (residues 305-307),
177 which together form a 9-residue internal β-hairpin (**Fig. 3b-c**). Notably, I305 is well-
178 resolved and located centrally in the 4-layer fold, pointed internally toward a 3-residue
179 hydrophobic groove in R4 (discussed below). R3 turns away from the 4-layer fold, forming
180 an 18-residue solvent-exposed β-hairpin (involving residues K317-G334). Alignment of
181 the Type I and II structures reveals they are nearly identical at the 4-layer fold and β-
182 hairpin regions (C_α root-mean-square deviation (RMSD) = 1.87 Å for residues K317-
183 G334). However, the C-terminal arm positions of Type I and Type II filaments are
184 substantially rotated (~100 deg) relative to each other due to a sharp kink in Type I
185 involving cross-β interactions D283:K369, S285:K369 and S285:G367 (**Fig. 3d**).
186

187 **Isoleucine Mutation and Additional Density Interaction Support a Structural Basis**
188 **of the S305I Tau Fold**

189 Based on the related neuropathological features between AGD and *MAPT S305I*
190 FTLD-tau[37], we next compared the S305I tau structures with the previously published
191 AGD structures[10]. Focusing on the predominant Type I folds, alignment reveals
192 substantial shifts in the overall structure and a more elongated solvent-exposed fold for
193 S305I (**Fig. 4a, Supplementary Video 1**). Beyond these limited similarities, the R3
194 hairpin, comprising residues 312-334, is the only conserved region between the sporadic
195 AGD and S305I structures. Residues 318-320 and 328-330 form a steric zipper in each
196 fold, and while the relative orientations are substantially rotated, the RMSD is <2.0 Å
197 between the two structures (**Fig. 4a, Extended Data Fig. 2**).

198 Notably, the large cavity, comprising R4-C and R2 in the AGD fold is collapsed in
199 the S305I structure with no additional internal density in this region (**Fig. 4a**). This enables
200 more continuous side chain interactions between R2 and R4, thereby elongating this stem
201 region. Moreover, in the S305I structure charged residues K290, K295, and N296 in R2
202 are reoriented toward the solvent-exposed face, where they, together with Y310 and K311,
203 coordinate the additional density located adjacent the R2–R3 junction (**Fig. 4b-c**). These
204 interactions would be incompatible with R2-R3 contacts observed in the AGD structure
205 and thus likely contribute to the rotated position of the R3 hairpin (**Fig. 4a**). Addtionally,
206 several charged residues in the C domain including K370 and E372 that are adjacent to
207 the additional density in the AGD strucure, are rotated and solvent exposed in the S305I
208 structure (**Fig. 4b-c**).

209 The 305 position lies at the junction of the R2 and R3 domains. In sporadic AGD,
210 S305 is located in a small Gly-rich turn comprised of residues H299-S305 and appears
211 to hydrogen bond with G303 in the adjacent strand (**Fig. 4b, top inset**). Model-building
212 indicated that Ile is physically incompatible with this conformation, eliminating the
213 interaction with G303 and sterically clashing with H299 (**Fig. 4b, bottom inset**).
214 Conversely, in the S305I structure, I305 faces into a hydrophobic groove in the center of
215 the 4-layer fold created by well-packed hydrophobic residues V337, V339, L344, and
216 F346 (**Fig. 4c, insets**). Importantly, these comparisons reveal that Ile mutation likely
217 contributes substantially to the overall fold we observe for the S305I structures.

218 Considering the large number of tau filament folds that have now been determined
219 and classified based on structural and neuropathological features[10], we next compared
220 the S305I fold to other disease-associated folds. To this end, we developed a comparison
221 method that evaluates the backbone RMSD between two aligned structures (e.g. S305I
222 Type I and sporadic AGD) over sliding windows of increasing sequence length, thereby
223 enabling the identification of regions with local structural similarity (See Methods). In
224 addition to generating RMSD values for all residue ranges, the results are visualized as
225 triangular heat-maps that highlight regions of structural correspondence across all
226 possible alignments between the two folds (**Extended Data Fig. 3**).

227 To identify tau filament structures most similar to the S305I Type I fold, we
228 calculated localized RMSD values for all currently available disease-associated tau folds
229 (**Table 2**), where localized RMSD is calculated as the average RMSD value over all
230 residue ranges in the structure. The comparison also uses sequence alignment for all
231 sequentially identical (or similar in the case of mutants) pairs of structures, allowing

232 different splicing forms to be compared. Unexpectedly, the AGD fold showed only
233 moderate similarity, whereas the MAPT P301T Type I[30] and sporadic CBD folds[13]
234 exhibited the greatest overall structural resemblance to the S305I fold (**Extended Data**
235 **Fig. 3**). Analysis of the heatmaps reveals distinct conserved motifs, including the R3
236 hairpin (residues ~312-334) and β-strand regions within R2 (~285-304) and R4-C (~354-
237 375) (**Extended Data Fig. 3b-c,e**). Among these, the R3 hairpin represents the most
238 consistently conserved structural element, present in AGD Type I, P301T Type I, and CBD
239 folds (**Extended Data Figs. 4**).

240 Solvent-accessible regions of R2 and R3 in both S305I filament types encase a
241 large well-defined density which extends along the length of the filament axis (**Fig. 5)**.
242 While the individual rungs of the density are well-defined, it contains connected regions
243 parallel to the filament axis. This density is positioned in a positively charged cleft flanked
244 by residues K290, K294, N296, Y310, and K311, indicating it is primarily negatively
245 charged (**Fig. 5a-b**). Given that it must satisfy multiple positive charges in each strand,
246 and from the cross-sectional view does not resemble a polypeptide, we hypothesize that
247 this density is a non-proteinaceous cofactor. The cofactor site (residues 290–311) is highly
248 conserved between Type I and Type II filaments (RMSD = 0.66 Å), which indicates that
249 the co-factor may also be conserved across the two filament types. This conserved region
250 extends from the middle of the R2 region to nearly the end of the R4 region (residues
251 290–364), with only small differences in backbone bending in the Z-plane (RMSD = 1.97
252 Å).

253 Unaccounted, likely non-proteinaceous densities have been observed in several
254 cryo-EM maps of other pathological tau fibrils[10,12,13]. These have been attributed to anions,

255 hydrophobic or charged metabolites or negatively charged RNA or polyphosphate that
256 bind to complementary regions of the fibril, potentially stabilizing the fold[10,12,13,44–46]. Thus,
257 there is growing interest in identifying these molecules as contributors to distinct tau folds,
258 however the densities are often diffuse and low-resolution, making their interaction difficult
259 to define. Notably, based on our RMSD analysis above, we identify the that P301T Type
260 I tau fold contains a region of strong structural homology compared to the S305I fold that
261 encompasses the R2–R3 junction (residues ~280-314) containing residue 305 and
262 residues K290, K294, N296, Y310 and K311 that coordinate the additional density
263 observed in our maps (**Extended Data Fig. 3e**)[30]. Upon examination of the deposited
264 P301T Type I map (EMD-51320), we identify a strikingly similar well-defined unaccounted
265 density in this region that is coordinated by the same residues we observe in the S305I
266 structures (**Extended Data Fig. 5**). We note this density was not previously reported for
267 the P301T Type I fold[30]. Based on these similarities, we propose that the additional
268 density in both structures likely corresponds to the same bound cellular metabolite or
269 polyanion. Together, these findings reveal structural commonalities between S305I and
270 other disease-associated tau folds and suggest that both the S305I substitution and the
271 associated bound factor together contribute to the distinct structural fold observed in
272 S305I.
273

274 **Molecular modeling and In vitro analysis indicate polyanions and S305I mutation**
275 **contribute to tau fibrilization.**

276 Based on the well-defined stacked arrangement of the extra density and positive
277 charge of the coordinating residues in the S305I structure, we next docked several

278 candidate molecules into the density (see Methods), to better understand potential
279 cofactor interactions (**Extended Data Fig. 6**). Based on the size of the density and
280 surrounding residues, we docked polyphosphate in addition to RNA and inositol
281 diphosphate[47], a common cellular metabolite containing two anionic phosphate groups,
282 into the density. Inositol diphosphate fits well in an arrangement in which the phosphate
283 groups interact with K290, K294, Y310, and K311, while the inositol rings stack together
284 along the fibril axis with a geometry that matches the overall 4.8 Å repeat of the amyloid
285 structure. A polyphosphate chain can dock into the density in straight or bent
286 configurations with the phosphate groups interacting with K294 and K311, but the fit is
287 incomplete with the chain accounting for only a fraction of the available density (**Extended**
288 **Data Fig. 6b-c**). We next docked poly-A and poly-G strands as a model for RNA. Poly-G
289 fits well in a single arrangement in which the phosphodiester backbone packs along the
290 fibril groove, interacting with K294, Y310, and K311, while the purine ring projects outward
291 at an angle that matches the density and enables an interaction with K290 (**Extended**
292 **Data Fig. 6d-g**). This stacked ring arrangement is similar to previous amyloid-small
293 molecule co-structures, in which pi-pi stacking between the aromatic rings of each ligand
294 supports interactions with the fibril[31,32,48]. We note that in all modeling tests, the
295 negatively-charged phosphodiester linkage is positioned in the cationic groove of the
296 S305I fibril, where it forms complementary electrostatic interactions with adjacent Lys
297 residues. Thus, this analysis further supports a direct role for polyanions such as RNA or
298 phosphate-containing metabolites functioning as cofactors that stably bind pathogenic
299 folds of tau.

300 Considering the Ile residue appears to directly organize the 4-layer tau fold of the
301 S305I structures we determined (**Fig. 4**), we hypothesized that the mutation itself may
302 contribute to disease pathology by promoting tau aggregation in addition to its reported
303 splicing defects and increased 4R tau expression[36,37]. To assess the impact of S305I on
304 tau aggregation, we compared the *in vitro* fibrilization kinetics of purified, recombinant
305 0N4R tau containing S305I or P301S, a well-characterized familial mutation known to
306 enhance aggregation, to wildtype, normal tau using an established Thioflavin T (ThT)
307 fluorescence assay[49,50]. Here we utilized polyphosphate, at 0.125 mg/mL, as an
308 established polyanion inducer of fibrilization[51] and determined the overall fibrillization rate
309 and aggregation propensity (as the inverse fluorescence half-time ($t_{1/2}$))[52], as described.
310 (**Fig. 6a and Extended Data Fig. 7**). Under these conditions, we observe that the S305I
311 fibrilization rate is significantly faster (by nearly 2-fold) compared to wildtype and slightly
312 faster than P301S (**Fig. 6b)**. Additionally, based on the aggregation propensity calculation,
313 S305I is modestly faster than wildtype while P301S is substantially faster (nearly 3-fold)
314 **(Fig. 6c)**. From this analysis, we conclude that the presence of the S305I mutation indeed
315 promotes tau aggregation, similar to what has been observed for other aggregation-prone
316 mutations such as P301S. Finally, we assessed the polyphosphate-induced S305I tau
317 fibrils by cryo-EM and identify they form intact twisted fibrillar structures that appear
318 distinct from other *in vitro* fibrils[53] (**Fig. 6d)**. Upon 2D classification analysis we identify
319 these fibrils are heterogeneous and adopt several different folds which prevented 3D
320 structure determination. However, several classes show a distinct curvature that appears
321 similar to the wavy morphology we observe for the brain-derived S305I fibrils indicating
322 some structural similarities may be present between these folds (**Extended Data Fig. 7d)**.

323

324 **Discussion**

325 Pathogenic mutations in the *MAPT* gene continue to be identified, with currently
326 over 60 linked to FTLD[54]. Many give rise to neuropathological phenotypes that closely
327 resemble those observed in well-characterized sporadic tauopathies, including AD, PSP,
328 CBD, and others[55]. On this basis, it has been proposed that distinct *MAPT* mutations can
329 be classified according to their corresponding sporadic tauopathy counterparts[24].
330 However, familial tauopathies often show earlier onset and greater severity than sporadic
331 forms, potentially driven by enhanced tau aggregation, excess 4R tau expression due to
332 intronic or silent mutations that disrupt intron 10 splicing, or other mechanisms[56–60].
333 Consequently, the influence of specific tau mutations on tau structure, aggregation
334 behavior, and disease phenotype remains unclear. Here we determined tau filament
335 structures from postmortem tissue of a patient with a rare *MAPT* familial FTLD mutation,
336 S305I, which resides at the exon 10 splice junction and is associated with severe early-
337 onset FTLD with pathological features that resemble AGD. Our structures reveal tau
338 S305I filaments adopt two related, but previously unreported 4-layer paired filament folds
339 involving tau repeat domain residues 273-379. The structures are distinct from sporadic
340 AGD, which is notable because of the related neuropathology including the presence of
341 tau deposits in the form of argyrophilic grains (**Fig. 1**). The Ile sidechain in the S305I fold
342 is efficiently packed in a hydrophobic cleft; the more polar Ser sidechain in the sporadic
343 AGD fold would be less well packed nor would it be hydrophobically stabilized. The
344 structure also contains an unidentified but well-defined density that stacks along an outer,
345 positively charged cleft, potentially also contributing to the unique fold. Notably, molecular

346 modeling indicates RNA or other phosphate-containing small-molecules could bind
347 favorably to the outer cleft and potentially account for the unidentified density, as has
348 previously been proposed for other tau structures[10,44,45]. Importantly, these structures add
349 to the diversity of tau folds that form in disease and reveal how a single mutation may
350 contribute mechanistically to FTLD.

351 Disease mutations at the 305 position and other sites in intron 10 are reported to
352 disrupt the RNA stem-loop structure at the splice junction, resulting in reduced splicing
353 and an overproduction of 4R tau relative to 3R[34,61]. However, differences in the clinical
354 and pathological features occur with these mutations, indicating that overproduction of
355 4R tau alone is not a predictor of specific pathology[61]. The *MAPT S305I* mutation, like
356 other 4R tau–associated tauopathies, presents with early-onset symptoms and rapid
357 progression[21,37,62] but exhibits AGD pathology distinct from other substitutions. S305N is
358 linked to Pick-like bodies composed of 4R tau[63], while the synonymous S305S
359 (AGT→AGC) shows PSP-like pathology[64]. Thus, these differences further indicate that
360 disease variation arises from mutation-specific effects beyond 4R tau overproduction.
361 Moreover, based on our structures, we predict S305N is unlikely to form the S305I tau
362 fold (**Extended Data Fig. 8**) due to asparagine's polar side chain pointed inward toward
363 the apolar pocket where I305 resides. Additionally, the S305N mutation is also
364 incompatible with the sporadic AGD fold, due to a 2.5 Å steric clash the asparagine's most
365 favorable rotamer makes with the H299 imidazole ring in chain *i+1* directly below. Thus,
366 we predict S305N likely adopts an additional unknown fold, that is associated with distinct
367 pathology and disease characteristics[30].

368 Structural determination of patient-derived tau filaments for 5 other familial *MAPT*
369 mutations has been achieved thus far. Some adopt folds previously identified in sporadic
370 tauopathies (ΔK281, V337M, R406W)[14,22], while others have unique folds (P301L and
371 P301T)[30]. Of the 3 familial disease folds that match sporadic diseases, only V337M is
372 located in the ordered filament core, and this mutation is both sterically and
373 electrostatically tolerated by the AD PHF fold[14]. In the P301L and P301T folds, which do
374 not match those of any sporadic diseases, the mutation of proline allows for an additional
375 hydrogen bond, potentially driving the formation of an alternative fold. The central position
376 of S305 in the 4-layer AGD fold and the destabilizing steric clash the mutant I305 has with
377 H299 in R2 (**Fig. 4b**) suggests that this mutation may play a more substantial role in
378 driving a specific tau fold compared to other mutations. To further understand the
379 relationship between tau mutations and fibrilization, we induced aggregation of WT, S305I,
380 and P301S tau via the addition of polyphosphate. S305I has a higher propensity to
381 aggregate and fibrilization rate relative to WT, further evidence the mutation itself may act
382 as a distinct driver of aggregation and the structural fold[14,22,30]. How the specific tau fold
383 and increased aggregation propensity of S305I mechanistically contribute to the
384 neuropathology and early disease onset characteristics of this FTLD remains to be
385 determined.

386 As there is often clinical and neuropathological overlap between familial and
387 sporadic forms of FTLD, the question as to whether these are familial versions of sporadic
388 tauopathies remains open and has important implications for the design of models,
389 diagnostics, and therapeutics for FTLD. Neuropathologically, S305I results in argyrophilic
390 grains resembling those found in AGD, which led to the hypothesis that this FTLD might

391 be a familial form of AGD[37]. Notable differences between FTLD-tau/*MAPT* S305I and
392 sporadic AGD, however, raised the possibility that they represent distinct diseases. The
393 pathology of sporadic AGD is primarily found in the limbic system, whereas S305I tau
394 inclusions extend much more widely. Glial characteristics also differ, with sporadic AGD
395 showing more prevalent granular-fuzzy type astroglial cytoplasmic inclusions. Recently,
396 comparison of filament folds has been suggested as a metric for classification of
397 tauopathies[10]. Given this, our structural findings demonstrate that S305I FTLD-tau is
398 distinct from AGD, as opposed to an early-onset form of the disease. As no broad
399 structural relationship has been established between FTLD-tau/*MAPT* and sporadic
400 tauopathies, further investigation is warranted regarding the classification of these
401 diseases.

402 Many amyloid filament structures from patients with tauopathies have shown
403 additional non-proteinaceous densities, indicating that the specific tau fold and its stability
404 may require the binding of distinct small-molecule metabolites or polyanions[10]. In Type I
405 and II sporadic AGD folds, a small, poorly resolved density is present in a solvent-
406 protected groove, interacting primarily with positively charged residues K294 and K370.
407 In S305I, both folds exhibit a collapse of this groove and the R2 strand with these residues
408 is flipped, introducing new sidechain interactions with R3 (**Fig. 4b-c)**. Notably, this R2-R3
409 interaction permits the formation of the solvent-exposed cleft in which K290, K294 and
410 N296 in R2, and Y310 and K311 in R3 together contact the exogenous molecules seen
411 as stacked density in the S305I folds. Interestingly, these same 5 residues in the P301T
412 fold form a very similar cleft that houses unassigned density which strongly resembles
413 that in the S305I folds[30]. Unassigned densities in these and other tauopathy filament folds

414 raise questions about the role and timing of these densities with respect to filament
415 formation. Upstream effects on cellular homeostasis could be driving specific filament
416 folds; alternatively, filaments could be sequestering small molecules after amyloid
417 formation. Irrespective of the temporal sequence, binding of a highly anionic molecule
418 would be expected to thermodynamically stabilize the conformation found in S305I fibrils.
419 Previous work has speculated that some of the unassigned densities in tau and other fibril
420 structures are associated with anionic molecules[10,65–68], including RNA[44]. This is
421 consistent with our modeling, which shows that multiple RNA molecules and other anions
422 fit the unassigned density in the S305I folds. Thus, it is of interest to identify the anionic
423 cofactors and elucidate their role in fibril formation and stabilization.
424

425 **Materials and Methods**

426

427 **Ethical review process and informed consent**

428 Human brain tissue samples were obtained from the Neurodegenerative Disease Brain
429 Bank at the University of California, San Francisco. Prior to autopsy, participants or their
430 surrogates provided informed consent for genetic testing and for brain donation, in
431 accordance with the principles of the Declaration of Helsinki. Procedures were approved
432 by the UCSF Committee on Human Research.
433

434 **Case materials**

435 Genetic screening was performed for common and rare FTD-related genes as
436 previously described[40]. Patient samples were screened by targeted sequencing of the

437 seven most common dementia-associated genes (microtubule-associated protein tau
438 [*MAPT*], progranulin [*GRN*], TAR DNA binding protein [*TARDBP*], fused in sarcoma [*FUS*],
439 amyloid beta precursor protein [*APP*], presenilin 1 [*PSEN1*], and presenilin 2 [*PSEN2*], as
440 described previously[40]. Coding and exon-intron boundary regions of these seven genes
441 were screened for known or novel (likely) pathogenic variants. Variants identified in the
442 screening were confirmed by Sanger sequencing[40].

443 Neuropathological diagnoses were made following consensus diagnostic
444 criteria[69–71] using previously described histological and immunohistochemical methods[72–
445 74]. Briefly, eight-micrometer thick sections were cut from formalin-fixed paraffin-embedded
446 blocks and stained with hematoxylin & eosin and with antibodies against
447 hyperphosphorylated tau (CP13, anti-mouse, 1:250, targeting pSer202, gift from Peter
448 Davies, Feinstein Institute for Medical Research, USA), amyloid-beta (anti-mouse, 1:500,
449 Millipore, MAB5206), TDP-43 (anti-rabbit, 1:4K, ProteinTech, 10782-2), alpha-synuclein
450 (anti-mouse, 1:5K, LB509, gift from John Trojanowski and Virginia Lee, University of
451 Pennsylvania, USA), and 3R-tau (anti-mouse, 1:2K, Millipore, 05-803) and 4R-tau (anti-
452 mouse, 1:2K, Millipore, 05-804), as described previously[72]. Cases were identified based
453 on neuropathological diagnosis and genetic screening. Photomicrographs of the
454 hyperphosphorylated tau-stained slides from the inferior frontal gyrus and inferior
455 temporal gyrus were captured using a digital camera (Nikon Digital Sight DS-Fi1)
456 mounted on a Nikon Eclipse 80i microscope using NIS-Elements (Version 3.22, Nikon)
457 imaging software. Fresh-frozen blocks of the inferior frontal gyrus and inferior temporal
458 gyrus were cut from freshly frozen coronal slabs that had been stored at -80 °C.
459

460 **Experimental design**

461 Samples were selected based on brain tissue availability and post-mortem
462 neuropathological examination. Sex was not considered in this study, as the structure of
463 AGD filaments does not vary by sex. Randomization and blinding were not performed in
464 this study, as there was only one patient available at the NDBB carrying the *S305I MAPT*
465 mutation.

466

467 **Tau Filament extraction**

468 Sarkosyl-insoluble material was extracted from the inferior frontal cortex using a protocol
469 similar to previous amyloid filament purifications[10]. In brief, tissues were homogenized in
470 20 volumes (v/w) of extraction buffer consisting of 10 mM Tris-HCl, pH 7.5, 0.8 M NaCl,
471 10% sucrose and 1 mM EGTA. Homogenates were brought to 2% sarkosyl and incubated
472 for 30 min at 37 °C. After a 10-min centrifugation at 20,000g at 4 °C, the supernatants
473 were spun at 100,000g at 4 °C for 20 min. The pellets were resuspended in 700 µL/g
474 extraction buffer and centrifuged at 9,500g for 10 min. The supernatants were diluted
475 threefold in 50 mM Tris-HCl, pH 7.5, containing 0.15 M NaCl, 10% sucrose and 0.2%
476 sarkosyl, and spun at 166,000g for 30 min. Sarkosyl-insoluble pellets were resuspended
477 in 25 µL/g of 20 mM Tris-HCl, pH 7.4 and 100 mM NaCl and used for cryo-EM.

478

479 **Negative stain imaging**

480 Purified frontal cortex tissue was diluted 1:10 for a final concentration of 150 µL/g frozen
481 tissue. 3 µL was added to a glow-discharged 400 mesh copper grid with a layer of
482 amorphous carbon. After 30 seconds, the grid was blotted with filter paper, washed, and

483 blotted twice with water. 4 µL of 0.75% uranyl formate was then added and blotted. Three
484 more 4 µL aliquots of uranyl formate were added and removed by vacuum aspiration.
485 Images were collected on a Talos L120C (Thermo Fisher Scientific) operating at 120 kV
486 and equipped with a Ceta-D (Thermo Fisher Scientific) camera.
487

488 **Cryo-EM grid preparation and data collection**

489 Extracted tau filaments were incubated at 37 °C in a 0.4 g/mL pronase solution for 30
490 minutes and centrifuged at 3,000 g for 5 minutes, then applied to glow-discharged holey
491 carbon grids (Quantifoil Au R1.2/1.3, 200 mesh). Then, 3 µL of purified tau filaments were
492 plunge-frozen in liquid ethane using a Vitrobot Mark IV System (Thermo Fisher Scientific).
493 Images were acquired on a 300 KeV Titan Krios microscope (Thermo Fisher Scientific)
494 equipped with a K3 direct electron-detection camera (Gatan, Inc.) with a BioQuantum
495 energy filter (Gatan, Inc.) with a slit width of 20 eV. Super-resolution movies were
496 recorded at 105,000x magnification (pixel size: 0.417 Å/pixel) with a defocus range of 0.8
497 to 1.8 µm and a total exposure time of 2.024 seconds fractionated into 0.025-second
498 subframes.
499

500 **Image Processing**

501 Datasets were processed in RELION using standard helical reconstruction[75]. The movies
502 were motion-corrected using MotionCor2[76] and Fourier-cropped by two to give the final
503 pixel size of 0.834 Å per pixel. The dose-weighted summed micrographs were directly
504 imported to RELION[77,78] and used for further processing. Contrast transfer function (CTF)
505 was estimated using CTFFIND 4.1[79]. The filaments were picked manually and extracted

with a box size of 900 pixels downsampled to 300 pixels. 2D classification was used to separate filamentous segments from junk particles, and then additional 2D classification was performed to distinguish Type I from Type II filament. 3D initial models were then created *de novo* from the 2D class averages using the crossover distances measured from the 2D class averages, 600 Å for type I and 750 Å for type II, using RELION's *relion_helix_inimodel2d* feature[80]. Particles associated with each filament type were re-extracted separately using a 300 pixel box, and 3D classification was performed using each initial model low-pass filtered to 15 Å. The best classes were selected from each 3D classification, and the final rise and twist was optimized in 3D auto-refinement. The final 3D densities were sharpened using standard postprocessing methods in RELION, and the final resolution was determined from Fourier shell correlation at 0.143 Å from two independently refined half-maps using a soft-edged solvent mask. The final resolution of the Type I filament was 3.1 Å and the resolution of the Type II filament was 3.2 Å.

Model Building and Refinement

The atomic model of the S305I and normal AGD structures were docked manually into the density using ChimeraX[81] and ISOLDE[42], using predicted models from ModelAngelo[43] as a guide. The model was refined against the density using Phenix. Figures were prepared using ChimeraX, PyMOL, and ABPS[82].

Filament Fold Comparison

527 Code was generated that evaluates the backbone RMSD between two filament folds over
528 sliding windows of increasing sequence length. Fully annotated code is available at
529 https://github.com/degrado-lab/amyloid_analysis.
530

531 **Docking of Polyanions**

532 Docking studies were performed using the Molecular Operating Environment (MOE;
533 Chemical Computing Group, Build MOE 2024.0601). The protein structure was derived
534 from the S305I Type I fold. The poly(A) RNA ligand was obtained from PDB entry 8ZWJ.
535 A poly(G) RNA model was generated by modifying the purine base of the poly(A) RNA
536 structure. Linear polyphosphate models were constructed in MOE, and a helical
537 polyphosphate model was generated by manually building the RNA phosphate backbone
538 followed by energy minimization. The inositol diphosphate structure was obtained from
539 PDB entry 1I9Z[83]. Docking was carried out using the MOE protein-protein docking module,
540 in which the ligand structures were sampled against the protein target. Candidate
541 complexes were generated through rigid-body placement followed by refinement and
542 scoring. The resulting docking poses were clustered base on interface interaction
543 fingerprints, and representative structures from the top-ranked clusters were selected for
544 further analysis.
545

546 **Recombinant protein expression and purification**

547 Recombinant 0N4R tau constructs were expressed from a pET-28a vector and
548 transfected into *Escherichia coli* BL21(DE3) plysS competent cells. Starter cultures
549 containing a single colony of transformed cells were grown in Terrific Broth (TB) containing

550 50 μg/mL kanamycin and 25 μg/mL chloramphenicol overnight (16-18 hours) at 37°C with
551 constant shaking at 200 rpm. Then, 15 mL of the starter culture was used to inoculate 1
552 L of terrific broth (TB), containing 50 μg/mL kanamycin and 25 μg/mL chloramphenicol.
553 Cell cultures (4 L per construct) were grown at 37°C with constant shaking at 200 rpm
554 until an optical density (OD_{600}) of 1.0 was reached. Expression was induced with 1 mM
555 IPTG for 16 hours at 16°C, then harvested by centrifugation (4000 rpm for 20 minutes)
556 and the cell pellets were flash frozen in liquid nitrogen.

557 To purify tau, cell pellets were resuspended in ice-cold lysis buffer (50mM MES pH
558 6.0, 20 mM NaCl, 2 mM DTT), supplemented with two cOmplete EDTA-free protease
559 cocktail inhibitor tablets (Roche). Cells were lysed by dounce homogenization and
560 sonication, and then boiled for 20 minutes at 80°C. The boiled lysate was clarified via
561 centrifugation at 30,000 g for 30 minutes. The clarified lysate was filtered using a 0.2-0.3
562 micron syringe filter and loaded onto a Cytiva CaptoS 5 mL column (GE healthcare)
563 equilibrated in a low salt buffer (50 mM MES pH 6.0, 20 mM NaCl, 2 mM DTT). The
564 sample was eluted using a 16-column volume (CV) gradient from 0% to 100% high salt
565 buffer (20 mM MES pH 6.0, 1.5 M NaCl, 2 mM DTT). Protein-containing fractions were
566 pooled and concentrated before loading into a 5 mL loop and injecting into a HiLoad
567 Superdex 200 16/600 column equilibrated with 1x PBS pH 7.4, 5% glycerol, 2 mM TCEP
568 for size-exclusion chromatography. Fractions containing protein were concentrated, flash
569 frozen, and stored at -80°C. Purity was analyzed via SDS-PAGE and final concentration
570 was verified via BCA assay (Pierce).

571

572 **Tau Fibrillization**

Aggregation reactions were performed in 384-well plates (Corning 4511). In each well, purified 10 μM 0N4R tau constructs (WT, P301S, S305I) were added to freshly prepared assay buffer (1x PBS pH 7.4, 2 mM TCEP). Aggregation was induced immediately prior to the start of the assay by adding polyphosphate at a final concentration of 0.125 mg/mL, with each well containing a total volume of 20 μL. Aggregation reactions were performed at 37°C with continuous shaking. Fluorescence measurements (excitation = 444 nm, emission = 475 nm, cutoff = 490 nm) were recorded in a Spectramax M5 microplate reader (Molecular Devices). Readings were taken every 5 minutes for at least 24 hours. Each experiment was performed with 9 replicate wells per condition, with 3 separate replicate experiments run.

Fibrilization Data Analysis

The first five data points were averaged and this background was subtracted from each sample. Baseline subtracted curves were fit using the Levenberg-Marquardt nonlinear least-squares method to the Gompertz function:

$$y(t) = Ae^{-e^{(t-t_i)/B}}$$

Where y is the fluorescent value at time (t), A is the amplitude of the curve, t_i is the inflection point, b is $1/k_{app}$ where k_{app} is the elongation constant. Individual experimental curves with max raw RFU values less than 50 and a mean-squared error (MSE) higher than 1 standard deviation of the mean of the maximum ThT signal were discarded. Analysis of the discarded curves shows features consistent with bubbles in reaction wells. Final data were plotted in GraphPad PRISM and with Matplotlib.

596 **Data Availability**

597 Cryo-EM maps and atomic coordinates have been deposited in the EMDB and PDB with
598 accession codes: EMD-75195 (Type I) and EMD-75196 (Type II), and PDB 10IJ (Type I)
599 and 10IK (Type II). Filament fold comparison code is available at
600 https://github.com/degrado-lab/amyloid_analysis. Any other relevant data are available
601 from the corresponding authors upon request.

602

603 **Acknowledgements**

604 This work was funded by the Rainwater Charitable Foundation (D.R.S.), and the National
605 Institutes of Health (P01AG002132: D.R.S. and W.F.D). The UCSF Neurodegenerative
606 Disease Brain Bank receives funding support from NIH grants P30AG062422,
607 P01AG019724, U01AG057195, and U19AG063911, as well as the Rainwater Charitable
608 Foundation and the Bluefield Project to Cure FTD. Data collection and dissemination of
609 the genetic data presented in this manuscript was supported by the ALLFTD Consortium
610 (U19: AG063911, funded by the National Institute on Aging and the National Institute of
611 Neurological Diseases and Stroke) and the former ARTFL & LEFFTDS Consortia (ARTFL:
612 U54 NS092089, funded by the National Institute of Neurological Diseases and Stroke and
613 National Center for Advancing Translational Sciences; LEFFTDS: U01 AG045390, funded
614 by the National Institute on Aging and the National Institute of Neurological Diseases and
615 Stroke). Additional funding support was provided by the National Institutes of Health (NIH)
616 National Institute on Aging (NIA) for Frontotemporal Dementia: Genes, Images, and
617 Emotions: P01 AG019724 and UCSF Alzheimer's Disease Research Center: P30
618 AG062422. Samples from the National Centralized Repository for Alzheimer's Disease

619 and Related Dementias (NCRAD), which receives government support under a
620 cooperative agreement grant (U24 AG21886) awarded by the National Institute on Aging
621 (NIA), were used in this study. The authors acknowledge the invaluable contributions of
622 the study participants and families as well as the assistance of the support staff at each
623 of the participating sites. H. S. P. received postdoctoral fellowship funding from the
624 BrightFocus Foundation (A141860). We thank Dr. Carlo Condello for his insight into the
625 fluorescence kinetic assay and unassigned density analysis.

626

627 **Author Contributions**

628 W.W.S., D.R.S., L.T.G., H.J.R., and M.L.G., and G.E.M conceptualized the study. H.S.P.,
629 G.E.M., W.W.S., D.R.S., and W.F.D. designed the experiments. H.S.P. and G.E.M.,
630 A.A.M., and E.T. performed cryo-EM sample preparation, data collection, and data
631 processing. H.S.P. generated atomic models on the basis of cryo-EM maps. A.N.L., S.S.,
632 E.M.R., A.L.L., and W.W.S. performed neurology, pathology, genetics and histology
633 studies. M.L., H.S.P., A.Y. and A.Q. cloned and purified recombinant tau constructs and
634 performed fibrilization assays. H.J. and H.S.P. performed docking studies. R.C.K. and
635 H.S.P. developed the code for structural homology analysis. H.S.P., G.E.M., A.N.L.,
636 W.W.S, and D.R.S. wrote and edited the manuscript.

637

638 **Ethics Declarations**

639 W.F.D. is a member of the scientific advisory boards of Alzheon Inc., Pliant, Longevity,
640 CyteGen, Amai, and ADRx Inc., none of which contributed support for this study. W.W.S
641 has received consulting fees from BridgeBio, Guidepoint Global, Inc., and GLG Council;

642 speaker honoraria from Verge Genomics; and compensation as a member of the scientific
643 advisory board for Lyterian Therapeutics, none of which contributed support for this study.
644 The remaining authors declare no competing interests.

645 **References**

646 1. Goedert, M., Spillantini, M. G., Cairns, N. J. & Crowther, R. A. Tau proteins of
647 alzheimer paired helical filaments: Abnormal phosphorylation of all six brain
648 isoforms. *Neuron* **8**, 159–168 (1992).

649 2. Buée-Scherrer, V. *et al.* Pathological τ proteins in postencephalitic Parkinsonism:
650 Comparison with Alzheimer's disease and other neurodegenerative disorders.
651 *Ann. Neurol.* **42**, 356–359 (1997).

652 3. Schmidt, M. L., Zhukareva, V., Newell, K. L., Lee, V. M. Y. & Trojanowski, J. Q.
653 Tau isoform profile and phosphorylation state in dementia pugilistica recapitulate
654 Alzheimer's disease. *Acta Neuropathol.* **101**, 518–524 (2001).

655 4. Crowther, R. A. Straight and paired helical filaments in Alzheimer disease have a
656 common structural unit. *Proc. Natl. Acad. Sci.* **88**, 2288–2292 (1991).

657 5. Flament, S., Delacourte, A., Verny, M., Hauw, J. J. & Javoy-Agid, F. Abnormal
658 Tau proteins in progressive supranuclear palsy. *Acta Neuropathol. 1991 816* **81**,
659 591–596 (1991).

660 6. Ksiezak-Reding, H. *et al.* Ultrastructure and biochemical composition of paired
661 helical filaments in corticobasal degeneration. *Am. J. Pathol.* **145**, 1496 (1994).

662 7. Togo, T. *et al.* Argyrophilic Grain Disease Is a Sporadic 4-Repeat Tauopathy. *J.*
663 *Neuropathol. Exp. Neurol.* **61**, 547–556 (2002).

664 8. Kovacs, G. G. *et al.* White Matter Tauopathy With Globular Glial Inclusions: A
665 Distinct Sporadic Frontotemporal Lobar Degeneration. *J. Neuropathol. Exp.*
666 *Neurol.* **67**, 963–975 (2008).

667 9. Delacourte, A. *et al.* Specific Pathological Tau Protein Variants Characterize

668 Pick's Disease. *J. Neuropathol. Exp. Neurol.* **55**, 159–168 (1996).
669 10. Shi, Y. *et al.* Structure-based classification of tauopathies. *Nature* **598**, 359–363
670 (2021).
671 11. Falcon, B. *et al.* Tau filaments from multiple cases of sporadic and inherited
672 Alzheimer's disease adopt a common fold. *Acta Neuropathol.* **136**, 699–708
673 (2018).
674 12. Falcon, B. *et al.* Novel tau filament fold in chronic traumatic encephalopathy
675 encloses hydrophobic molecules. *Nat. 2019 5687752* **568**, 420–423 (2019).
676 13. Zhang, W. *et al.* Novel tau filament fold in corticobasal degeneration. *Nature* **580**,
677 283–287 (2020).
678 14. Qi, C. *et al.* Tau filaments with the Alzheimer fold in human MAPT mutants
679 V337M and R406W. *Nat. Struct. Mol. Biol. 2025* 1–8 (2025) doi:10.1038/s41594-
680 025-01498-5.
681 15. Ghosh, U. *et al.* Cryo-EM structures reveal tau filaments from Down syndrome
682 adopt Alzheimer's disease fold. *Acta Neuropathol. Commun.* **12**,
683 2024.04.02.587507 (2024).
684 16. Fitzpatrick, A. W. P. *et al.* Cryo-EM structures of Tau filaments from Alzheimer's
685 disease brain. *Nature* **547**, 185 (2017).
686 17. Falcon, B. *et al.* Structures of filaments from Pick's disease reveal a novel tau
687 protein fold. **561**, (2018).
688 18. Spillantini, M. G. & Goedert, M. Tau protein pathology in neurodegenerative
689 diseases. *Trends Neurosci.* **21**, 428–433 (1998).
690 19. Alzheimer's Disease Genetics Fact Sheet | National Institute on Aging.

691 https://www.nia.nih.gov/health/alzheimers-causes-and-risk-factors/alzheimers-
692 disease-genetics-fact-sheet.
693 20. Greaves, C. V. & Rohrer, J. D. An update on genetic frontotemporal dementia. *J.*
694 *Neurol.* **266**, 2075 (2019).
695 21. Giannini, L. A. A. *et al.* Isoform-specific patterns of tau burden and neuronal
696 degeneration in MAPT-associated frontotemporal lobar degeneration. *Acta*
697 *Neuropathol.* **144**, 1065–1084 (2022).
698 22. Schweighauser, M. *et al.* Mutation ΔK281 in MAPT causes Pick's disease. *Acta*
699 *Neuropathol.* **146**, 211–226 (2023).
700 23. Dickson, D. W., Kouri, N., Murray, M. E. & Josephs, K. A. Neuropathology of
701 Frontotemporal Lobar Degeneration–Tau (FTLD-Tau). *J. Mol. Neurosci.* **45**, 384
702 (2011).
703 24. Forrest, S. L. *et al.* Retiring the term FTDP-17 as MAPT mutations are genetic
704 forms of sporadic frontotemporal tauopathies. *Brain* **141**, 521–534 (2018).
705 25. Hoerndli, F. J., Pelech, S., Papassotiropoulos, A. & Götz, J. Aβ treatment and
706 P301L tau expression in an Alzheimer's disease tissue culture model act
707 synergistically to promote aberrant cell cycle re-entry. *Eur. J. Neurosci.* **26**, 60–72
708 (2007).
709 26. Yoshiyama, Y. *et al.* Synapse Loss and Microglial Activation Precede Tangles in a
710 P301S Tauopathy Mouse Model. *Neuron* **53**, 337–351 (2007).
711 27. Allen, B. *et al.* Abundant Tau Filaments and Nonapoptotic Neurodegeneration in
712 Transgenic Mice Expressing Human P301S Tau Protein. *J. Neurosci.* **22**, 9340–
713 9351 (2002).

714 28. Schweighauser, M. *et al.* Cryo-EM structures of tau filaments from the brains of
715 mice transgenic for human mutant P301S Tau. *Acta Neuropathol. Commun.* **11**,
716 1–11 (2023).
717 29. Ayers, J. *et al.* Severe neurodegeneration in brains of transgenic rats producing
718 human tau prions. *Acta Neuropathol.* **148**, 1–22 (2024).
719 30. Schweighauser, M. *et al.* Distinct tau filament folds in human MAPT mutants
720 P301L and P301T. *Nat. Struct. Mol. Biol. 2025* 1–9 (2025) doi:10.1038/s41594-
721 025-01575-9.
722 31. Merz, G. E. *et al.* Stacked binding of a PET ligand to Alzheimer's tau paired
723 helical filaments. *Nat. Commun. 2023 141* **14**, 1–11 (2023).
724 32. Kunach, P. *et al.* Cryo-EM structure of Alzheimer's disease tau filaments with PET
725 ligand MK-6240. *Nat. Commun. 2024 151* **15**, 1–7 (2024).
726 33. Josephs, K. A. *et al.* Flortaucipir PET uncovers relationships between tau and
727 amyloid-β in primary age–related tauopathy and Alzheimer's disease. *Sci. Transl.*
728 *Med.* **16**, 8076 (2024).
729 34. Spillantini, M. G. & Goedert, M. Tau mutations in familial frontotemporal dementia.
730 *Brain* **123**, 857–859 (2000).
731 35. Chen, S., Townsend, K., Goldberg, T. E., Davies, P. & Conejero-Goldberg, C.
732 MAPT Isoforms: Differential Transcriptional Profiles Related to 3R and 4R Splice
733 Variants. *J. Alzheimer's Dis.* **22**, 1313 (2010).
734 36. Bowles, K. R. *et al.* Development of MAPT S305 mutation human iPSC lines
735 exhibiting elevated 4R tau expression and functional alterations in neurons and
736 astrocytes. *Cell Rep.* **43**, (2024).

737 37. Kovacs, G. G. *et al.* MAPT S305I mutation: Implications for argyrophilic grain
738 disease. *Acta Neuropathol.* **116**, 103–118 (2008).
739 38. Rodriguez, R. D. & Grinberg, L. T. Argyrophilic grain disease: An underestimated
740 tauopathy. *Dement. Neuropsychol.* **9**, 2–8 (2015).
741 39. Steele, N. Z. *et al.* Frequency of frontotemporal dementia gene variants in
742 C9ORF72, MAPT, and GRN in academic
743 versus commercial laboratory cohorts. *Adv. Genomics Genet.* **Volume 8**, 23–33
744 (2018).
745 40. Ramos, E. M. *et al.* Genetic screening of a large series of North American
746 sporadic and familial frontotemporal dementia cases. *Alzheimer's Dement.* **16**,
747 118–130 (2020).
748 41. Yokota, O. *et al.* Amygdala granular fuzzy astrocytes as lesions preceding
749 development of argyrophilic grains: data from 239 autopsy cases. *Free
750 Neuropathol.* **3**, 18 (2022).
751 42. Croll, T. I. ISOLDE: A physically realistic environment for model building into low-
752 resolution electron-density maps. *Acta Crystallogr. Sect. D Struct. Biol.* **74**, 519–
753 530 (2018).
754 43. Jamali, K. *et al.* Automated model building and protein identification in cryo-EM
755 maps. *Nat. 2024 6288007* **628**, 450–457 (2024).
756 44. Abskharon, R. *et al.* Cryo-EM structure of RNA-induced tau fibrils reveals a small
757 C-terminal core that may nucleate fibril formation. *Proc. Natl. Acad. Sci. U. S. A.*
758 **119**, e2119952119 (2022).
759 45. Huettemann, P. *et al.* Amyloid Accelerator Polyphosphate Implicated as the

760 Mystery Density in α-Synuclein Fibrils. *bioRxiv* 2024.05.01.592011 (2024)
761 doi:10.1101/2024.05.01.592011.
762 46. Huettemann, P. *et al.* Amyloid accelerator polyphosphate fits as the mystery
763 density in α-synuclein fibrils. *PLOS Biol.* **22**, e3002650 (2024).
764 47. Shears, S. B. Diphosphoinositol Polyphosphates: Metabolic Messengers? *Mol.*
765 *Pharmacol.* **76**, 236 (2009).
766 48. Shi, Y. *et al.* Cryo-EM structures of tau filaments from Alzheimer's disease with
767 PET ligand APN-1607. *Acta Neuropathol.* **141**, 697–708 (2021).
768 49. Allen, B. *et al.* Abundant Tau Filaments and Nonapoptotic Neurodegeneration in
769 Transgenic Mice Expressing Human P301S Tau Protein. *J. Neurosci.* **22**, 9340–
770 9351 (2002).
771 50. Berriman, J. *et al.* Tau filaments from human brain and from in vitro assembly of
772 recombinant protein show cross-β structure. *Proc. Natl. Acad. Sci. U. S. A.* **100**,
773 9034–9038 (2003).
774 51. Montgomery, K. M. *et al.* Chemical Features ofPolyanions Modulate Tau
775 Aggregationand Conformational States. *J. Am. Chem. Soc.* **145**, 3926 (2023).
776 52. Mok, S. A. *et al.* Mapping interactions with the chaperone network reveals factors
777 that protect against tau aggregation. *Nat. Struct. Mol. Biol.* **25**, 384–393 (2018).
778 53. Zhang, W. *et al.* Heparin-induced tau filaments are polymorphic and differ from
779 those in alzheimer's and pick's diseases. *Elife* **8**, 1–24 (2019).
780 54. Shafei, R. *et al.* Two pathologically confirmed cases of novel mutations in the
781 MAPT gene causing frontotemporal dementia. *Neurobiol. Aging* **87**, 141.e15-
782 141.e20 (2020).

783 55. Strang, K. H., Golde, T. E. & Giasson, B. I. MAPT mutations, tauopathy, and
784 mechanisms of neurodegeneration. *Lab. Investig.* **99**, 912–928 (2019).
785 56. Hutton, M. *et al.* Association of missense and 5′-splice-site mutations in tau with
786 the inherited dementia FTDP-17. *Nat. 1998 3936686* **393**, 702–705 (1998).
787 57. Ando, K. *et al.* de novo MAPT mutation G335A causes severe brain atrophy, 3R
788 and 4R PHF-tau pathology and early onset frontotemporal dementia. *Acta*
789 *Neuropathol. Commun. 2020 81* **8**, 94- (2020).
790 58. Qian, W. & Liu, F. Regulation of alternative splicing of tau exon 10. *Neurosci. Bull.*
791 *2014 302* **30**, 367–377 (2014).
792 59. Holmes, B. B. *et al.* Proteopathic tau seeding predicts tauopathy in vivo. *Proc.*
793 *Natl. Acad. Sci. U. S. A.* **111**, E4376–E4385 (2014).
794 60. Sanders, D. W. *et al.* Distinct Tau Prion Strains Propagate in Cells and Mice and
795 Define Different Tauopathies. *Neuron* **82**, 1271–1288 (2014).
796 61. Goedert, M. *et al.* Tau Protein and Frontotemporal Dementias. *Adv. Exp. Med.*
797 *Biol.* **1281**, 177–199 (2021).
798 62. Saito, Y. *et al.* Staging of Argyrophilic Grains: An Age-Associated Tauopathy. *J.*
799 *Neuropathol. Exp. Neurol.* **63**, 911–918 (2004).
800 63. Kobayashi, K. *et al.* Pick's Disease Pathology of a Missense Mutation of S305N of
801 Frontotemporal Dementia and Parkinsonism Linked to Chromosome 17: Another
802 Phenotype of S305N. *Dement. Geriatr. Cogn. Disord.* **17**, 293–297 (2004).
803 64. Skoglund, L. *et al.* The tau S305S mutation causes frontotemporal dementia with
804 parkinsonism. *Eur. J. Neurol.* **15**, 156–161 (2008).
805 65. Yao, Q. Q., Hong, L., Wu, S. & Perrett, S. Distinct microscopic mechanisms for

806 the accelerated aggregation of pathogenic Tau mutants revealed by kinetic
807 analysis. *Phys. Chem. Chem. Phys.* **22**, 7241–7249 (2020).
808 66. Schweighauser, M. *et al.* Structures of α-synuclein filaments from multiple system
809 atrophy. *Nature* **585**, 464–469 (2020).
810 67. Yang, Y. *et al.* Structures of α-synuclein filaments from human brains with Lewy
811 pathology. *Nature* **610**, (2022).
812 68. Yang, Y. *et al.* New SNCA mutation and structures of α-synuclein filaments from
813 juvenile-onset synucleinopathy. *Acta Neuropathol.* **145**, 561–572 (2023).
814 69. Ferrer, I., Santpere, G. & Van Leeuwen, F. W. Argyrophilic grain disease. *Brain*
815 **131**, 1416–1432 (2008).
816 70. MacKenzie, I. R. A. *et al.* Nomenclature and nosology for neuropathologic
817 subtypes of frontotemporal lobar degeneration: An update. *Acta Neuropathol.*
818 **119**, 1–4 (2010).
819 71. Montine, T. J. *et al.* National institute on aging-Alzheimer's association guidelines
820 for the neuropathologic assessment of Alzheimer's disease: A practical approach.
821 *Acta Neuropathol.* **123**, 1–11 (2012).
822 72. Kim, M. *et al.* Diagnosis of Alzheimer Disease and Tauopathies on Whole-Slide
823 Histopathology Images Using a Weakly Supervised Deep Learning Algorithm.
824 *Lab. Investig.* **103**, 100127 (2023).
825 73. Kim, E. J. *et al.* Selective frontoinsular von economo neuron and fork cell loss in
826 early behavioral variant frontotemporal dementia. *Cereb. Cortex* **22**, 251–259
827 (2012).
828 74. Tartaglia, M. C. *et al.* Sporadic corticobasal syndrome due to FTLD-TDP. *Acta*

829 *Neuropathol.* **119**, 365–374 (2010).
830 75. He, S. & Scheres, S. H. W. Helical reconstruction in RELION. *J. Struct. Biol.* **198**,
831 163–176 (2017).
832 76. Zivanov, J., Nakane, T. & Scheres, S. H. W. A Bayesian approach to beam-
833 induced motion correction in cryo-EM single-particle analysis. *IUCrJ* **6**, 5–17
834 (2019).
835 77. He, S. & Scheres, S. H. W. Helical reconstruction in RELION. *J. Struct. Biol.* **198**,
836 163–176 (2017).
837 78. Kimanius, D., Dong, L., Sharov, G., Nakane, T. & Scheres, S. H. W. New tools for
838 automated cryo-EM single-particle analysis in RELION-4.0. *Biochem. J.* **478**,
839 4169–4185 (2021).
840 79. Rohou, A. & Grigorieff, N. CTFFIND4: Fast and accurate defocus estimation from
841 electron micrographs. *J. Struct. Biol.* **192**, 216–221 (2015).
842 80. Scheres, S. H. W. Amyloid structure determination in RELION-3.1. *Acta*
843 *Crystallogr. Sect. D Struct. Biol.* **76**, 94–101 (2020).
844 81. Pettersen, E. F. *et al.* UCSF ChimeraX: Structure visualization for researchers,
845 educators, and developers. *Protein Sci.* **30**, 70–82 (2021).
846 82. Baker, N. A., Sept, D., Joseph, S., Holst, M. J. & McCammon, J. A. Electrostatics
847 of nanosystems: Application to microtubules and the ribosome. *Proc. Natl. Acad.*
848 *Sci. U. S. A.* **98**, 10037–10041 (2001).
849 83. Tsujishita, Y., Guo, S., Stolz, L. E., York, J. D. & Hurley, J. H. Specificity
850 Determinants in Phosphoinositide Dephosphorylation: Crystal Structure of an
851 Archetypal Inositol Polyphosphate 5-Phosphatase. *Cell* **105**, 379–389 (2001).

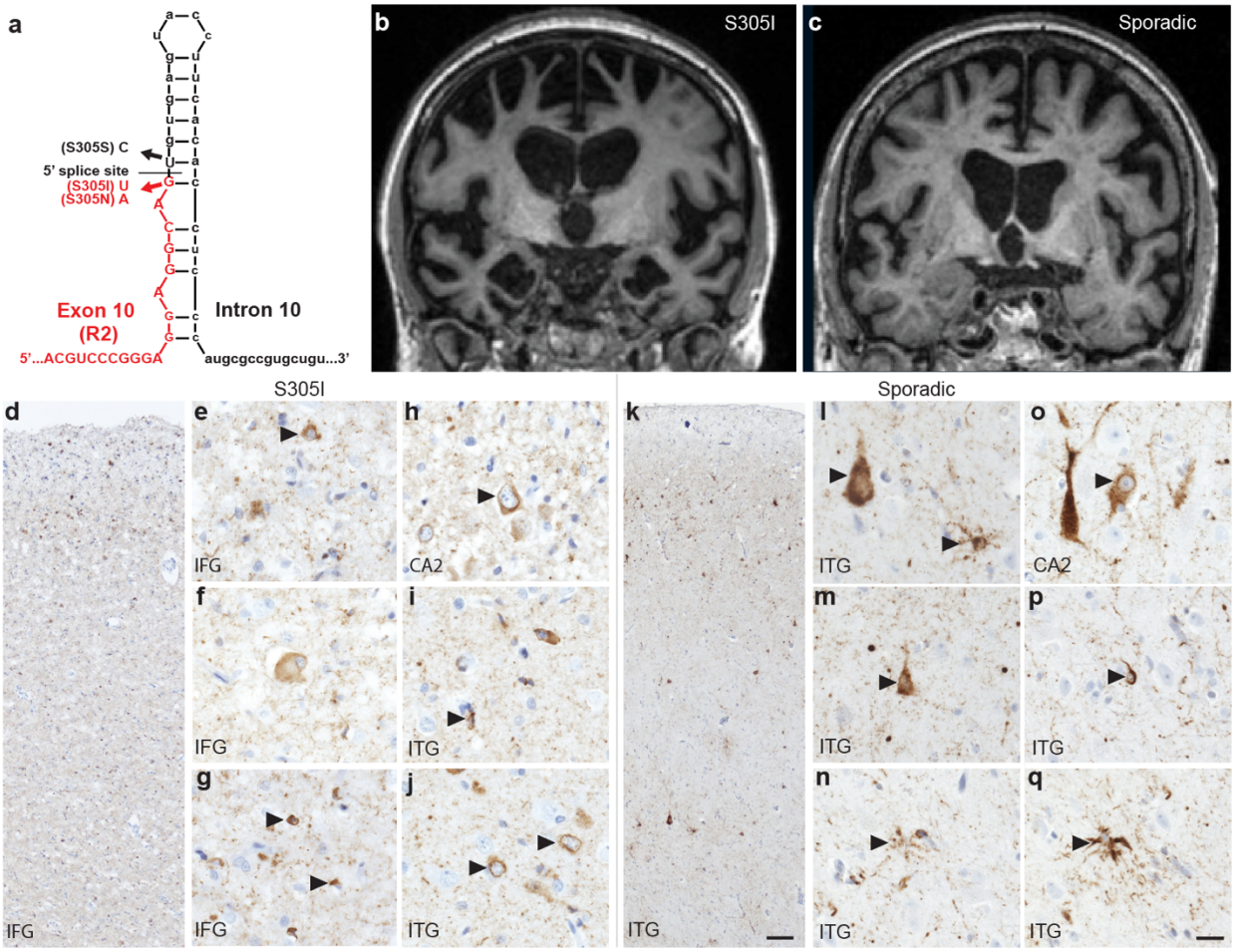

852

Figure 1: The *MAPT S305I* mutation and neuropathology. a, Schematic showing the location of *S305I* (with *S305S* and *S305N*) in the *MAPT* gene at the exon 10 (red) and intron 10 (black) splice-site junction and stem loop region. **b, c,** MRI scans from the patient carrying the S305I mutation (**b**) and a patient with sporadic AGD (**c**), shown for comparison. **d-q,** Representative images of immunostaining for phospho-tau (S202, CP13 antibody) in the patient carrying an S305I mutation **d-j,** and the patient with sporadic AGD **k-q**. Features of AGD are indicated by arrowheads in the inferior frontal gyrus (IFG, **d-g**), the CA2 region of the hippocampus (**h, o**), and the inferior temporal gyrus (ITG, **i-n, p, q**). Shared features characteristic of AGD include diffuse/granular cytoplasmic inclusions with perinuclear halos (**e, h, j, l, m, o**), and coiled bodies (**g, i, p**). Distinguishing features include ballooned neurons in the S305I case (**f**) and granular/fuzzy astrocytic inclusions in sporadic AGD (**l, n, q**). Scale bar in **k** = 100 μm and applies to **d** and **k**, and scale bar in **q** = 20 μm and applies to **e-j** and **l-q**.

853

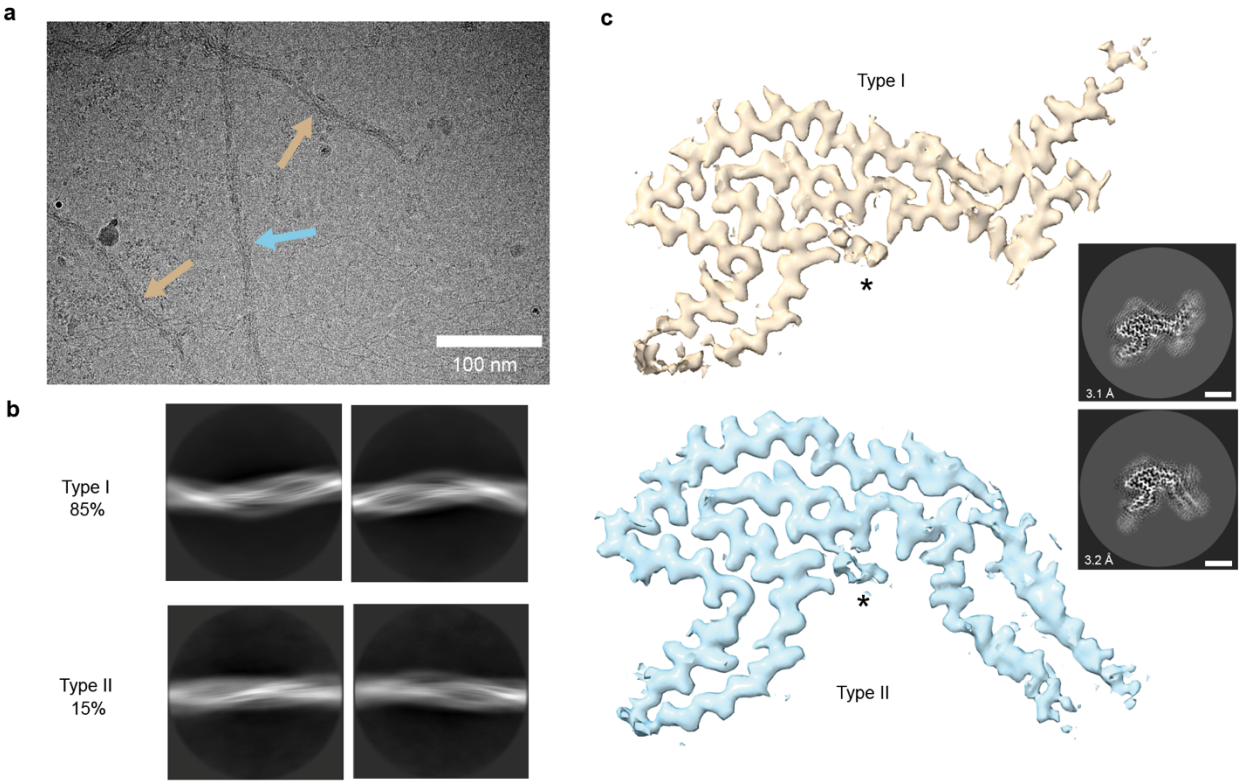

854

Figure 2: Cryo-EM 2D characterization and 3D structures identifying distinct S305I tau filament folds. a, Representative cryo-EM micrograph showing Type I (beige arrows) and Type II filaments (light-blue arrow). Scale bar equals 100 nm. **b,** Representative 2D class averages of Type I (top) and Type II (bottom) folds (with a 750 Å box size) showing distinct wavy morphologies. **c,** Cryo-EM final maps of S305I Type I (top, beige) and Type II (bottom, light-blue) tau filaments with additional, unaccounted density shown (*) and corresponding 2D cross-sections with resolution and particle percentages indicated for each final map shown (3.1 Å with 85% of the data for Type I and 3.2 Å with 15% for the data for Type II). Scale bars equal 30 Å.

855

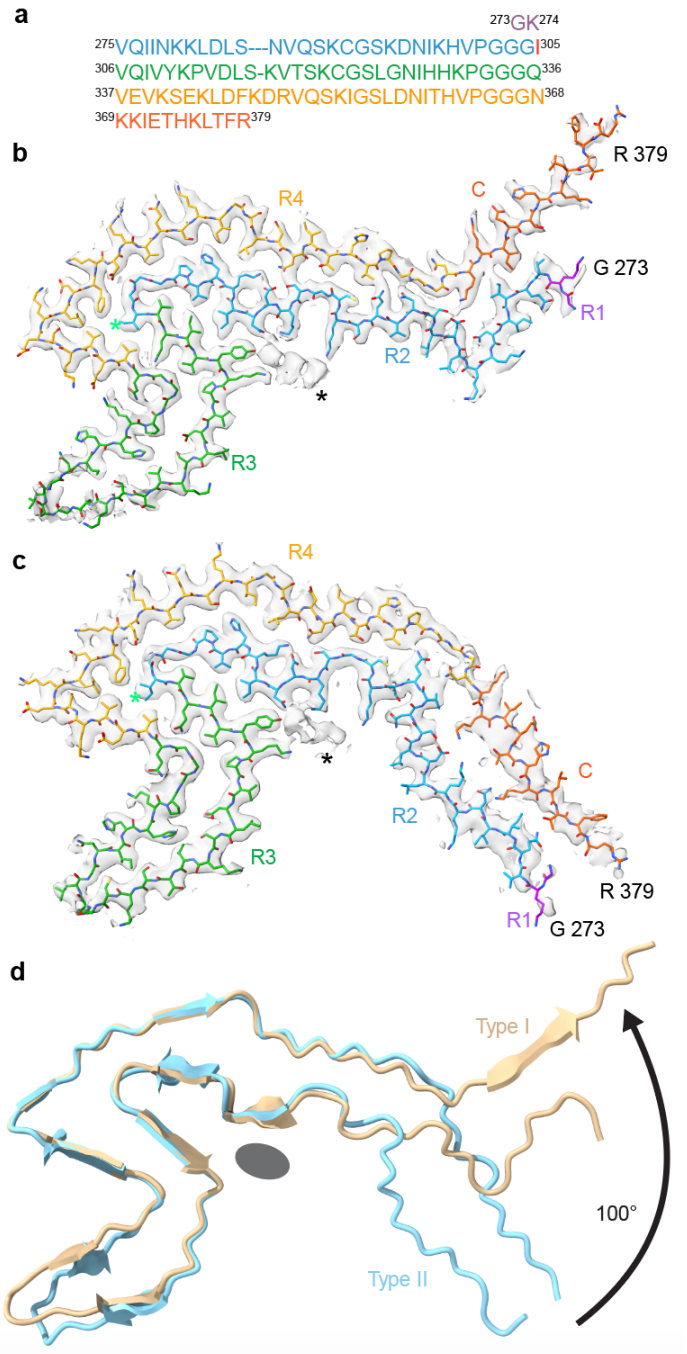

856

Figure 3: Cryo-EM atomic models and comparison of Type I and Type II S305I folds. a, Amino acid sequence and color scheme of the tau structural core that includes R1–R4 residues 273–368 (colored magenta, blue, green, and gold, respectively), and C-terminal residues 369-379 (orange) with S305I highlighted in red. **b-c,** Cryo-EM filament cross-section map/models of Type I (**b**) and Type II (**c**), colored by domain as in (**a**) with unassigned density shown for both filament types (*). **d,** α-carbon backbone overlay of Type I (beige) and Type II (light blue) folds showing 100° rotated position of the R2-C arm and overlapping position of the unassigned density (grey oval).

857

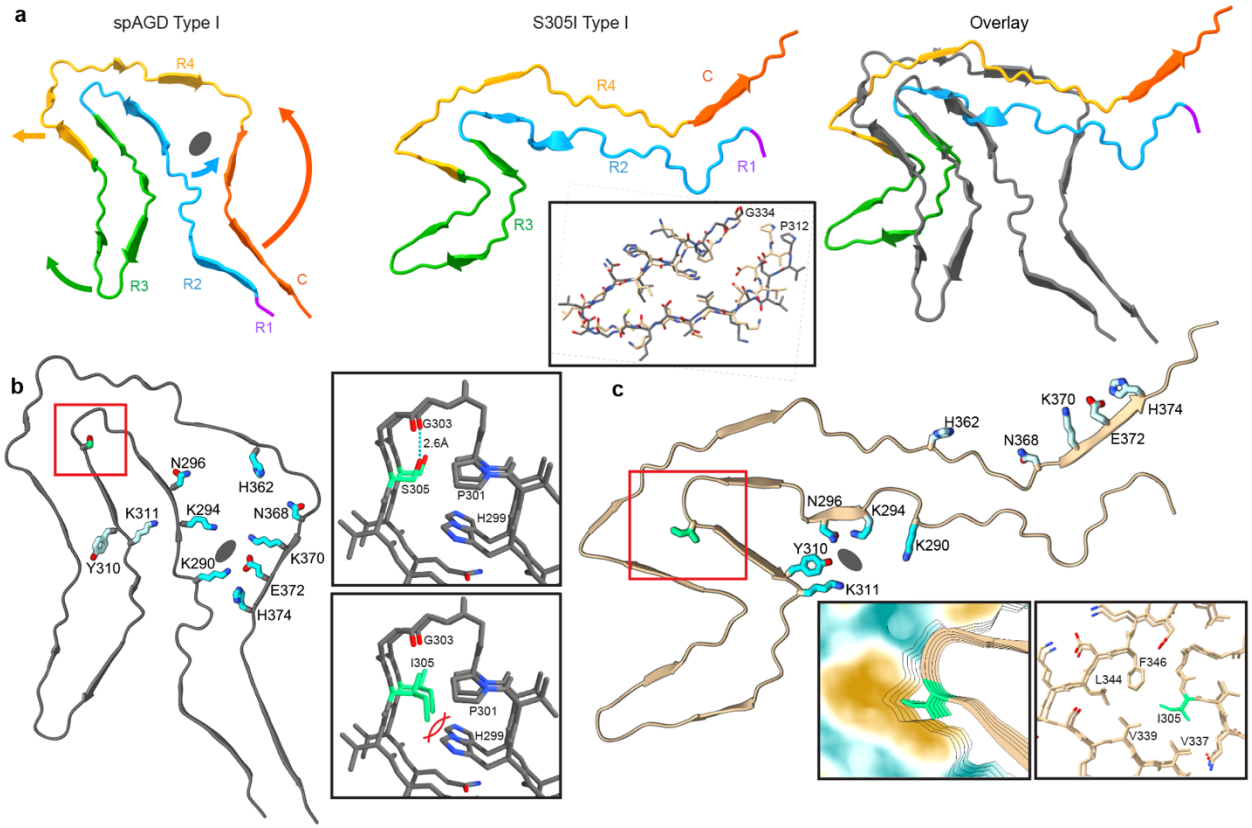

Figure 4: Structure comparison and organization at position 305 for sporadic AGD and S305I Type I filament folds. a, The spAGD Type I fold (left), colored as in Fig. 2a with arrows indicating major rearrangements in comparison to S305I Type I (middle), and an overlay of the two structures aligned to R4, with AGD in grey. **b,** The spAGD structure showing solvent-inaccessible polar residues (teal) that form a cavity around an unassigned density (grey oval), and the S305 position (red square). Top inset shows S305 (green) hydrogen bonding with G303; bottom inset shows the incompatibility of a theoretical I305 arrangement in the AGD fold due to a clash with H299. **c,** The S305I structure showing the same polar residues are rotated outward and solvent-accessible, with K294, N296, Y310 and K311 interacting with the unassigned density (grey oval) bound to the outside of the filament. The I305 region is identified (red square) and enlarged with a surface view showing the Ile position in a hydrophobic cleft (left inset) and the surrounding pocket formed by residues V337, V339, L344, and F346 (right inset).

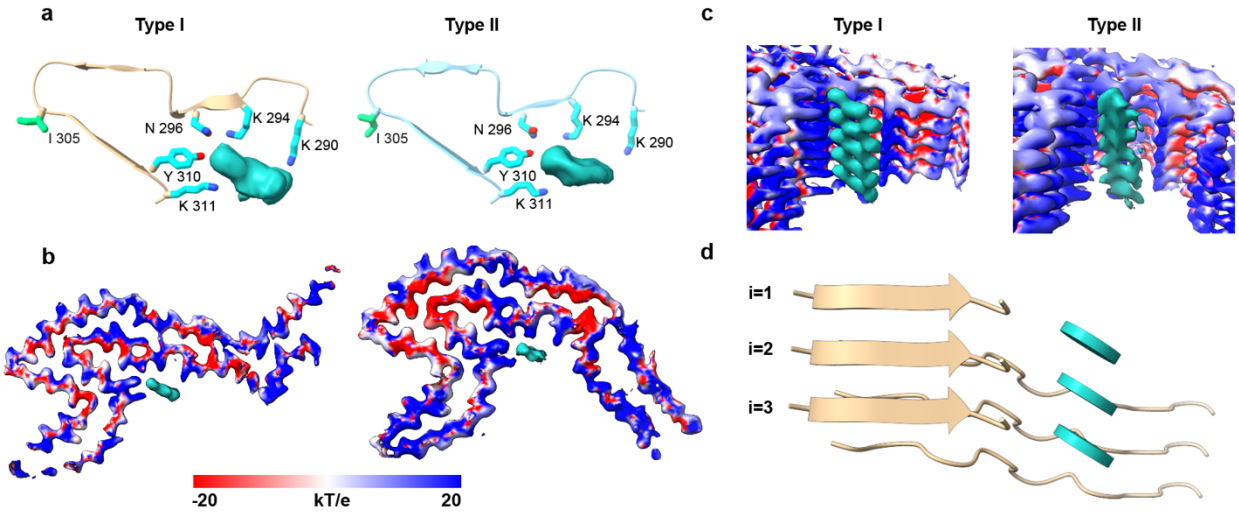

Figure 5: Comparison of unassigned density in both S305I folds; cryo-EM density of S305I Type I (beige) and Type II (light-blue) filaments highlighting the unassigned density along the fibril axis. The unassigned density, which may house a shared cofactor, is shown in cyan. a, Top views of the S305I Type I (top) and Type II (bottom) filament residues surrounding the unassigned density. **b,** Top-down views of the unassigned density in the S305I Type I (top) and Type II (bottom) density maps, with electrostatic surfaces colored blue and red to indicate positively and negatively charged regions, respectively. **c,** Side views of the unassigned density in the S305I Type I (top) and Type II (bottom) density maps, with electrostatic surfaces colored blue and red to indicate positively and negatively charged regions, respectively. **d,** Side view of the predominant S305I Type I fibril and a planar representation of the hypothesized cofactor within the unassigned density along the length filament.

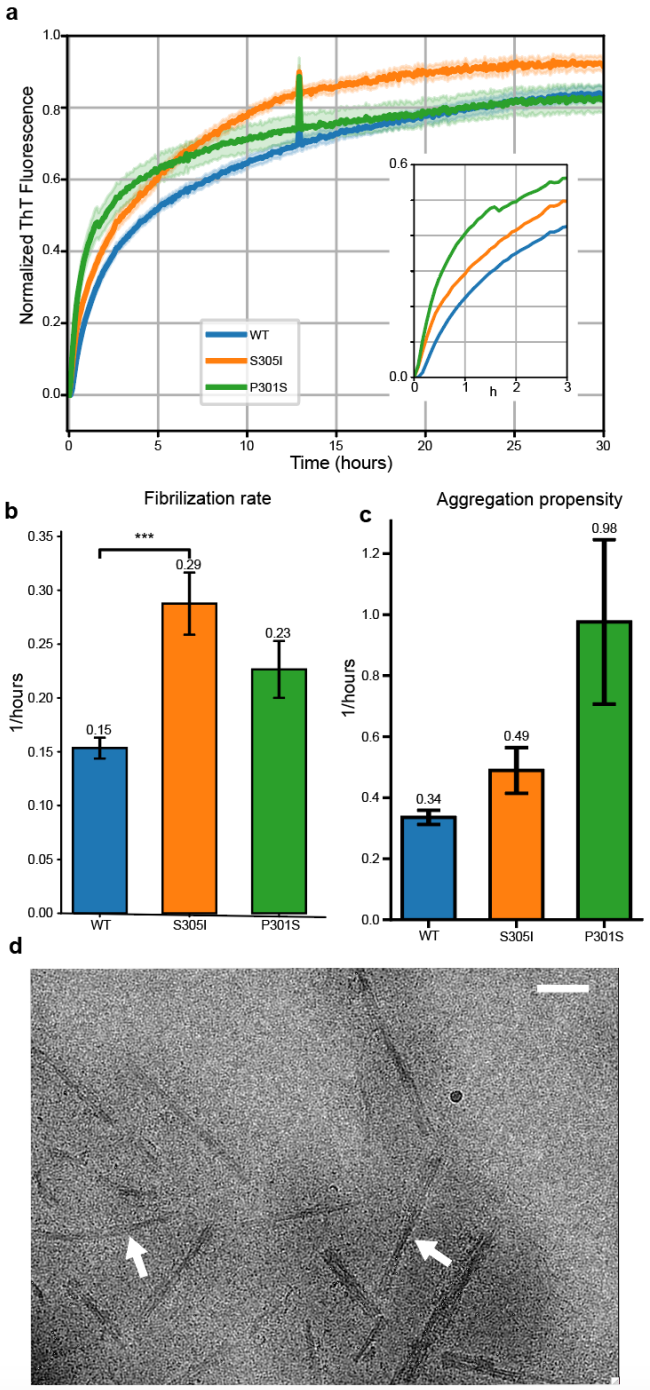

Figure 6: Increased *in vitro* fibrilization of S305I tau. **a,** Fibrilization curves for WT (blue), S305I (orange) and P301S (blue) 0N4R tau, using polyphosphate as the inducer. **b,** Filament elongation rate, calculated from the Gompertz function (see Methods). S305I is significantly faster than WT, as determined by a one-way ANOVA with Dunnett's post-hoc test. **c,** Aggregation propensity for each construct, calculated as the inverse $t_{1/2}$. **d,** Representative cryo-electron micrograph of recombinant S305I tau following polyphosphate-induced aggregation showing well-resolved twisted filaments (arrows) (Scale bar = 50 nm).